A&A 382, 984–998 (2002)
DOI: 10.1051/0004-6361:20011655

Astronomy & Astrophysics

Multi-wavelength spectrophotometry of EX Hydrae⋆

S. Eisenbart, K. Beuermann, K. Reinsch, and B. T. Gänsicke

Universitäts-Sternwarte, Geismarlandstr. 11, 37083 Göttingen, Germany

Received 1 October 2001 / Accepted 16 November 2001

Abstract. We present phase-resolved infrared and optical spectrophotometry of the intermediate polar EX Hya supplemented by archival ultraviolet data. The spin-modulated emission from the accretion funnel and the emission from the accretion disk or ring contain substantial optically thin components. The white dwarf dominates the unmodulated flux in the ultraviolet and is identified by numerous absorption lines. Metal absorption in the accretion curtain may add to the observed spectral features. The secondary star is of spectral type M4 ± 1 and is detected by its ellipsoidal modulation. We derive a distance of 65 ± 11 pc which makes EX Hydrae one of the closest cataclysmic variables with a known distance. The luminosity derived from the integrated overall spectral energy distribution is 3×10^{32} erg s^{-1}. The accretion rate of 3×10^{15} g s^{-1} (for an 0.6 $M_\odot$ white dwarf) is in reasonable agreement with the rates expected from angular momentum loss by gravitational radiation and from the observed spin-up of the white dwarf.

Key words. stars: individual: EX Hydrae – cataclysmic variables – accretion

1. Introduction

EX Hya was discovered by Kraft (1962) and quickly recognised as an eclipsing system with an orbital period $P_{\rm orb} = 98$ min. A second prominent periodicity $P_{\rm spin} = 67$ min was interpreted as the rotation period of the white dwarf (Vogt et al. 1980; Kruszewski et al. 1981) which led to the intermediate polar model of EX Hya (Warner 1983). X-ray emission in the quiescent state was discovered by Watson et al. (1978), a hard X-ray eclipse was first seen by Beuermann & Osborne (1985, 1988).

In this paper, we report new phase-resolved infrared and optical spectrophotometry. We have identified the secondary star in the infrared and use its K-band flux to determine the distance to EX Hya, a key parameter for the discussion of its luminosity and accretion rate. The derived distance is smaller than thought previously, requiring a current accretion rate of only 3×10^{15} g s^{-1} (for an 0.6 $M_\odot$ white dwarf), consistent with the rates expected from gravitational radiation and implied by the observed spin-up of the white dwarf (Hellier & Sproats 1992). Combining our data with archival IUE and HST spectrophotometry, we determine the contributions to the overall flux distribution from the rotating funnel, the accretion disk or ring, and the white dwarf. The short-wavelength ultraviolet spectrum contains metal absorption lines which are a clear signature of the white dwarf and/or absorption in the accretion funnel which surrounds the white dwarf. Based on these findings, we discuss the overall energy balance and present an internally consistent description of EX Hya as an intermediate polar.

Send offprint requests to: K. Beuermann,
e-mail: beuermann@uni-sw.gwdg.de

⋆ Based on observations made at the European Southern Observatory, Chile, with the ESO/MPI 2.2-m telescope in MPI time and at the Cerro Tololo Interamerican Observatory, Chile, under ESO programme ID 59.D-0724, and on observations made with the NASA/ESA Hubble Space Telescope, obtained from the Data Archive at the Space Telescope Science Institute, which is operated by the Association of Universities for Research in Astronomy, Inc., under NASA contract NAS 5-26555.

2. Observations and data analysis

2.1. Observations and archival data

We have observed EX Hya in February 1997 during three subsequent nights in the near infrared (0.8–2.4 μm) with the Infrared Spectrometer (IRS) at the 4-m telescope of the Cerro Tololo Interamerican Observatory (CTIO) and during one night in the optical (3600–10 200 Å) with the ESO Faint Object Spectrograph and Camera 2 (EFOSC 2) at the ESO/MPI 2.2 m telescope at La Silla. We complemented these data by archival time-resolved ultraviolet spectrophotometry taken with HST and IUE in 1995. Table 1 summarizes the relevant information. During all observations EX Hya was in a quiescent state. For comparison and calibration purposes in the near infrared and optical ranges, spectra of several M dwarfs with spectral types between dM2 and dM5.5 and of an A0 standard star were taken.

Table 1. Summary of time-resolved observations used for the present analysis. $t_{\rm int}$ and $t_{\rm res}$ are the exposure times and and the effective time resolution. The values quoted for the HST FOS data refer to time-averaged spectra (see text).

Telescope	Instrument	λ (Å)	date / UT	$t_{\rm int}$ (s)	$t_{\rm res}$ (s)	Observer
CTIO 4-m	IRS	8200–24 200	Feb. 22/23 1997 05:55–09:55 Feb. 23/24 1997 07:35–09:20 Feb. 24/25 1997 07:00–09:55	60	65	K. Reinsch S. Eisenbart
ESO 2.2-m	EFOSC2	3600–10 200	Feb. 28/Mar 1 1997 06:50–08:50	240	∼360	K. Reinsch S. Eisenbart
IUE	SWP	1150–1980	Jun. 23 1995, 13:50 – Jun 24 1995, 20:30	600	∼2400	K. Mukai
HST	FOS	1160–1600	Feb. 12 1995 04:05–14:20 Feb. 15 1995 12:30–22:40	3.34	∼13.3	S. R. Rosen

2.1.1. IRS

The IRS at CTIO is a cooled grating spectrometer equipped with a two-dimensional InSb detector array which allows spectral resolutions of $\lambda/\Delta\lambda \approx 150...3000$ in the wavelength range 0.8–5 μm (Depoy et al. 1990). When used by us, it was upgraded compared to Depoy et al. We chose a setup which allowed to observe the whole wavelength range of 8300–24 200 Å with a spectral resolution of $\lambda/\Delta\lambda \simeq 560$ and a time resolution of 65 s. The seeing was 1.0″–1.3″ during the first and 1.2″–1.8″ during the second and third night. A fraction of the observation time in nights 2 and 3 was affected by clouds and the spectra taken during these times were discarded. All spectra were obtained through a 2″ aperture.

A total of 222 useful spectra of EX Hya were taken, the majority during the first night. In order to correct the spectra for water vapor absorption in the infrared, we observed the nearby G5 star SAO 181198 at regular intervals. The NIR spectrum of this star has virtually no intrinsic spectral features apart from the hydrogen lines and the hourly spectra taken of this star allow a correction for H_2O absorption, at least on this time scale.

The M dwarfs observed were Gl 382 (dM2), Gl 443 (dM3), Gl 402 (dM4), Gl 285 (dM4.5e), and Gl 473AB (dM5.5e). As for EX Hya, spectra of nearby G0–G5 stars were taken for correction purposes.

2.1.2. EFOSC 2

The optical spectra were taken a few days after the infrared observations when EX Hya was practically at the same brightness level. The sky was clear with a seeing of 1.7″. We observed EX Hya through a 2″ slit with low spectral resolution (EFOSC2 grating G1, $\lambda/\Delta\lambda \simeq 150$) covering the wide wavelength range from 3600 to 10 200 Å. A total of 20 spectra were taken with an integration time of 4 min and an effective time resolution of 6 min. They cover 1.2 orbital or 1.7 spin cycles and include two eclipses.

2.1.3. IUE

From the IUE data archive, we selected a continuous set of 45 SWP spectra ($\lambda = 1150$–1980 Å) obtained by K. Mukai over 1.3 days in June 1995. They are the same spectra used by Mauche (1999) in his analysis of EX Hya. The spectra were taken through the large aperture with an exposure time of 600 s ($\Delta\phi_{67} = 0.15$). For further description of the data including a list of the phases of the individual spectra see Mauche (1999). The SWP spectra were supplemented by long-wavelength spectra which are effectively not spin-resolved, however.

2.1.4. HST

From the HST archive, we obtained two sets of spectra taken by S. R. Rosen with the Faint Object Spectrograph (FOS) on Feb. 12 and 15, 1995. The spectra were obtained with the G130H grating and the 4.3″ aperture covering the wavelength range 1160–1600 Å at a FWHM resolution of 1.5 Å. There are 14 data sets of 120 spectra each which extend over orbital phases $\phi_{98} = -0.15$ to $+0.20$ and thereby cover 14 eclipses. The data were taken with the FOS operated in rapid readout mode at an integration time of 3.34 s, resulting in an effective time resolution of 13.3 s. In order to improve the S/N ratio of the individual spectra, we averaged 12 subsequent spectra and thus reduced each of the 14 data sets to 10 spectra with a $S/N \simeq 8$ and an effective time resolution of 160 s. We note that the eclipse in EX Hya of about 3 min full width is seen in the original data, but is lost at the reduced time resolution.

2.2. Data analysis

The IUE and HST data required no further reduction, except for the removal of small spectral sections in the IUE data which were affected by reseau marks. The optical spectra were processed with standard MIDAS routines. The data structure and the intense sky background of the

infrared spectra required special routines which one of us (SE) developed and integrated into MIDAS.

Absolute flux calibration of near IR spectra is difficult because suitable spectrophotometric standard stars are rare. To overcome this problem, we took spectra of several A-type photometric standard stars. The near IR spectra of such stars are blackbody-like and almost featureless except for H and He absorption lines. This allows us to construct the intrinsic spectrum of each star as a blackbody for the effective temperature of its spectral type and to reproduce observed photometric *JHK* magnitudes by appropriate least-squares scaling. In all cases, the colours of the constructed spectra agreed with the literature values to better than ± 0.05 mag. Finally, the individual spectral response functions derived from the constructed and the observed spectra agreed with each other to within a few percent over the whole wavelength range. Using this procedure, the mean atmospheric absorption in the object spectra is already accounted for in the spectral response function. The remainder was removed using the spectra of the "monitor" stars mentioned in Sect. 2.1.1.

3. Light curve analysis

EX Hya shows variations on the 67-min spin period and on the 98-min orbital period. For the light curve analysis, we used the orbital and spin ephemerides of Hellier & Sproats (1992), including the sinusoidal term in the former. Both ephemerides are given in Julian Days and refer to the barycentric dynamical time definition. Phase $\phi_{98} = 0$ indicates the center of the optical (and X-ray) eclipse and phase $\phi_{67} = 0$ the maximum of the optical (and X-ray) flux during the spin cycle. We confirm the finding by other authors (Hurwitz 1997; Mauche 1999; Mukai et al. 1998) that the orbital ephemeris needs an update (the eclipse appears at $\phi_{98} = -0.02$ instead of at 0.00. This small deviation is not of relevance for the present study.

The flux-calibrated time-resolved spectra allow an analysis of the spectral variations as a function of phase and a light curve analysis for finite bands in wavelength. We start here with the light curve analysis.

From the individual spectra, we extract the time dependence of the total fluxes in broad bands (dominated by the continuum) and of the fluxes in the prominent emission lines above the continuum. The optical and IR broad bands approximately agree with Bessell *UBVRI* and Johnson *IJHK*, respectively, while the ultraviolet bands were, in part, chosen to be free of emission lines. We fit the individual data trains of the continuum and the emission line fluxes with model light curves of the form

$$\begin{aligned} F(t) = C + B\,t &+ A_{67} \cos 2\pi\,(\phi_{67}(t) + \Delta\phi_{67}) \\ &+ A_{98} \cos 2\pi\,(\phi_{98}(t) + \Delta\phi_{98}) \\ &- A_{49} \cos 2\pi\,(\phi_{49}(t) + \Delta\phi_{49}) \end{aligned} \quad (1)$$

where the term $B\,t$ accounts for a slow variation of the mean flux over the observation time, A_{67}, A_{98}, and A_{49} are the amplitudes of the modulations at the spin, the orbital, and half the orbital period, ϕ_{67}, ϕ_{98}, and ϕ_{49} are the corresponding phases, and $\Delta\phi_{67}$, $\Delta\phi_{98}$, and $\Delta\phi_{49}$ the phase shifts relative to the ephemerides of Hellier & Spoats (1992). (Note that a phase shift $\Delta\phi_{49} = 0.02$ corresponds to a shift by 0.01 orbital periods.) The only significant modulation in the ultraviolet occurs at the spin period. Spin modulation is also dominant in the optical and our data train is too short to obtain meaningful parameters for modulation at the other periods. Only the longer time coverage in the infrared allows to deduce the modulation at all three periods provided for in Eq. (1). Tables 2 and 3 list the least-squares fit parameters. Of the emission lines, $P\gamma$ is covered, too, but can not sufficiently well be separated from HeI λ10830. The mean visual and K-band fluxes in Table 2 correspond to mean magnitudes of EX Hya of $V = 13.43$ and $K = 11.77$ at the time of our observations.

3.1. Spin modulation

Figure 1 (upper panels) show examples of the IUE fluxes fitted with line 1 of Eq. (1): (i) the total flux in the 1250–1950 Å range and (ii) the emission line flux of CIV λ1550. Both fits benefit from including the term $B\,t$ in Eq. (1). We conclude that there is a gradual increase of the ultraviolet flux over the time of the observation on top of the spin modulation. The folded data, after subtraction of the linear term, $A + B\,t$, are shown in the lower panels. Tables 2 and 3 list the mean spectral fluxes f, the integrated line fluxes F, the corresponding amplitudes A_{67}, phase shifts $\Delta\phi_{67}$, and the corresponding fractional modulations, e.g., $\mathcal{M}_{67} = 2\,A_{67}/f_{\max}$, where $f_{\max}$ is the mean spectral flux at spin maximum. $\mathcal{M}_{67} = 1$ corresponds to 100% modulation and $\mathcal{M}_{67} > 1$ for SiIII λ1300 implies that the line which is in emission at spin maximum turns into absorption at spin minimum. Allowance for a time-dependent amplitude would further improve the fit in Fig. 1, but complicate the definition of the modulation amplitude. The HST data yield very similar spin modulation but do not require the term $B\,t$. The modulation of the line fluxes exceeds the modulation of the continuum in the HST and IUE data as well as in the optical data (Tables 2 and 3).

The infrared data continue the decline in the amplitude of the spin modulation seen in the optical bands. Figure 2 shows the result for the K-band (left top panel) and the $P\beta$ line (right top panel). Optical depth effects in the infrared emission line region are important as indicated by $B\gamma$. This line displays practically zero spin modulation of the integrated line flux (Table 2), but varies in width such that broad emission lines with deep absorption cores appear in the spin-modulated spectral flux (spin maximum – spin minimum). Figure 3 (bottom panel) shows $B\gamma$ and the absorption cores of the higher Brackett lines up to B13. Such effects are still present in $P\beta$ and decrease in the higher Paschen lines.

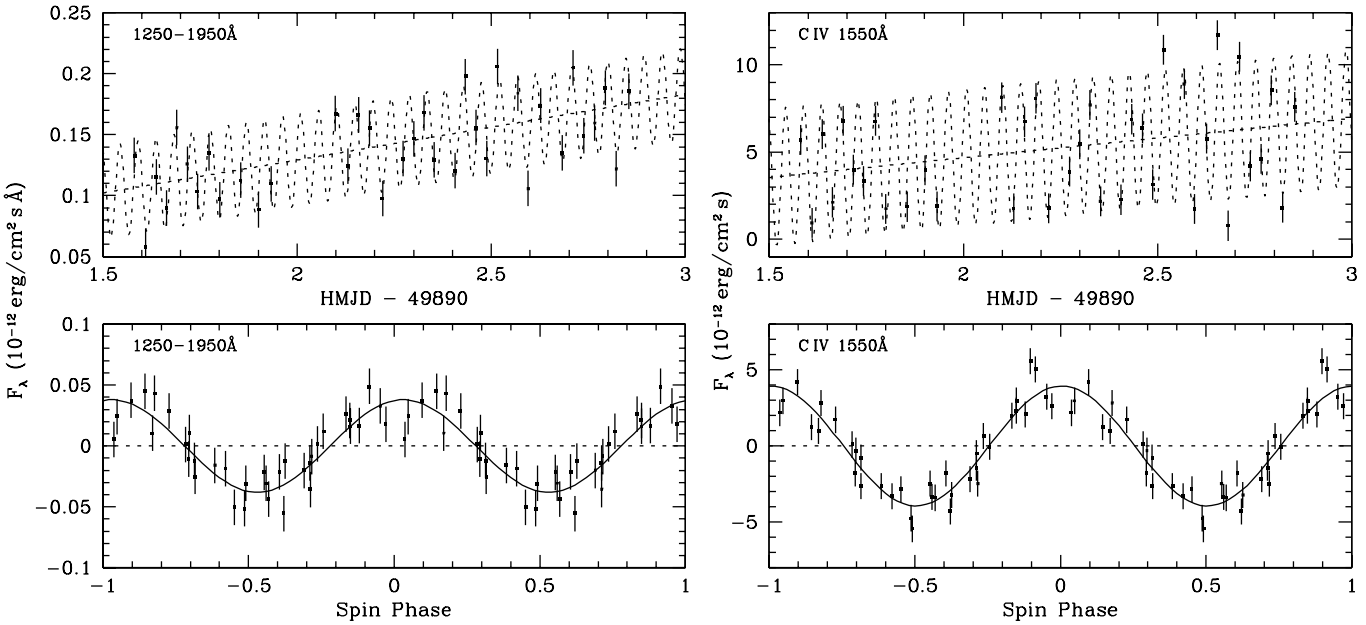

Fig. 1. Fits of line 1 of Eq. (1) to sample IUE light curves of EX Hya. *Left panel:* total flux in the 1250–1950 Å band, *right panel:* C IV λ1550 emission line flux. *Top panels:* original time series and fitted model, *bottom panels:* data with the linear term $A + B\,t$ subtracted and folded over the 67-min spin phase.

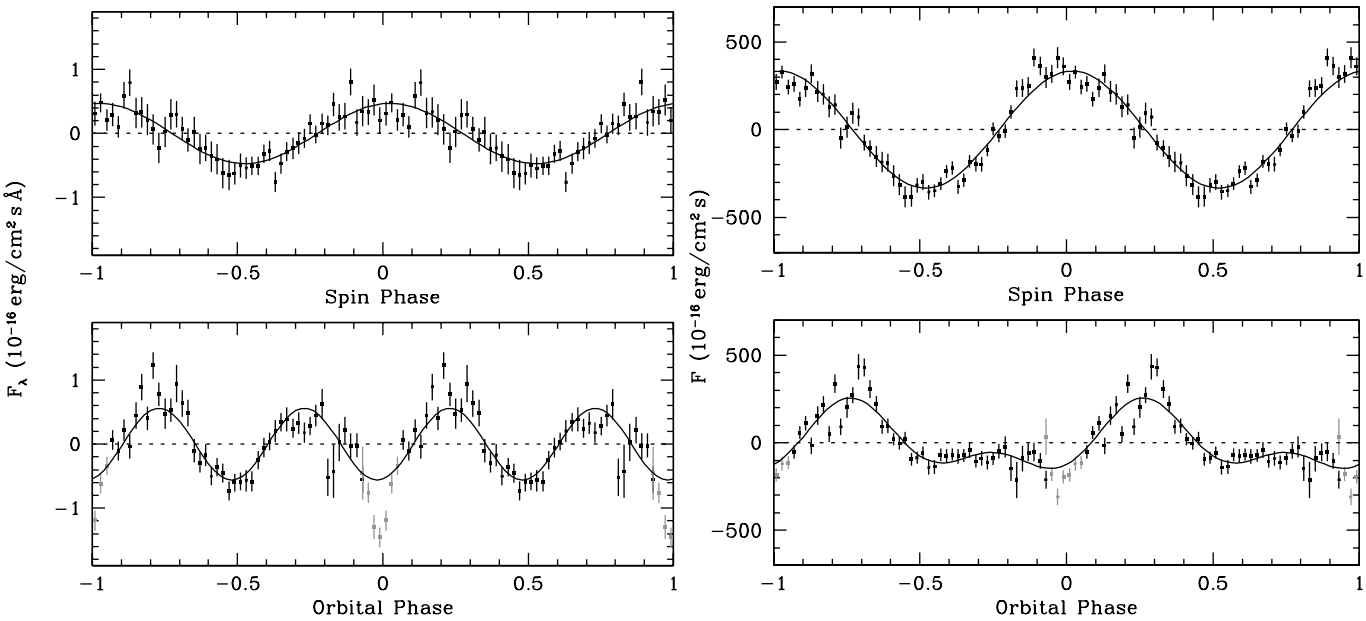

Fig. 2. *Left panels:* spin and orbital modulation of EX Hya in the IR (quasi $K-$band: 20 000–24 000 Å). The data points around the eclipse (grey) were excluded from the fits. *Right panels:* same for the Paschen Pβ line. The fit in the lower right panel represents the sum of the modulations at the orbital and half the orbital period.

3.2. Orbital modulation

In our optical spectrophotometry, the orbital eclipse occurs slightly early at $\phi_{98} = 0.98$. There is an indication for a shallow maximum near $\phi_{98} \simeq 0.8$ as shown to be present by Hellier et al. (2000; see also Siegel at al. 1989). The light curves of the Balmer line fluxes are flat and show a weak broad eclipse, as expected if part of the emission line fluxes originates from the accretion disk or ring.

Our infrared continuum data (lower left panel of Fig. 2) show the orbital eclipse superposed on substantial modulation at half the orbital period (data points covering the eclipse are displayed in gray). The infrared eclipse is more pronounced at spin maximum than at spin minimum, but is present at all spin phases. At the same time, the infrared eclipse is much wider than the eclipses at all other wavelengths, indicating that a much more extended structure than just the accretion funnel is partially eclipsed. The full width of about 10 min corresponds to an eclipsed object of

Table 2. Mean spectral fluxes f in box-car shaped wavelength intervals and amplitudes of modulation at the spin A_{67} in units of 10^{-16} erg cm^{-2} s^{-1} Å^{-1}. $\Delta\phi_{67}$ is the shift in the spin maximum relative to the ephemeris of Hellier & Spoats (1992) and $\mathcal{M}_{67}$ the modulation amplitude defined in the text. The lower section gives the corresponding information for the modulation at half the orbital period in the infrared.

$\lambda\lambda$ (Å)	f	A_{67}	$\Delta\phi_{67}$	$\mathcal{M}_{67}$
a) Hubble Space Telescope:				
1255–1285	1480	319 ± 24	−0.010	0.355
1350–1365	1590	276 ± 22	+0.01	0.296
1350–1380	1630	304 ± 23	+0.005	0.314
1425–1525	1500	221 ± 19	+0.005	0.256
1570–1600	1360	261 ± 17	+0.015	0.323
b) International Ultraviolet Explorer:				
1255–1285	1450	264 ± 40	+0.05	0.308
1350–1380	1560	356 ± 60	+0.015	0.372
1425–1525	1440	211 ± 52	+0.02	0.256
1575–1625	1220	250 ± 49	+0.035	0.341
1680–1780	1030	262 ± 35	+0.025	0.407
1875–1975	1030	283 ± 39	+0.025	0.430
c) ESO EFOSC2:				
3600–4000	539	140 ± 18	+0.03	0.411
3900–5000	286	59 ± 11	+0.035	0.342
5000–6200	155	26 ± 6	+0.05	0.287
5800–8000	121	22 ± 4	+0.04	0.312
7500–10 000	75	11.4 ± 2.4	+0.04	0.265
d) Cerro Tololo IRS:				
9650–10 650	52.0	5.28 ± 0.32	+0.035	0.184
11 000–13 500	37.6	3.31 ± 0.22	+0.03	0.162
14 500–18 000	18.5	1.34 ± 0.10	+0.03	0.135
20 000–24 000	8.3	0.47 ± 0.05	+0.025	0.107
$\lambda\lambda$ (Å)	f	A_{49}	$\Delta\phi_{49}$	$\mathcal{M}_{49}$
9650–10 650	52.0	2.39 ± 0.34	−0.005	0.088
11 000–13 500	37.6	2.16 ± 0.23	−0.02	0.109
14 500–18 000	18.5	1.21 ± 0.11	−0.03	0.123
20 000–24 000	8.3	0.56 ± 0.05	−0.04	0.127

Table 3. Mean integrated line fluxes F and modulation amplitudes A_{67} in units of 10^{-16} erg cm^{-2} s^{-1}. $\Delta\phi_{67}$ and $\mathcal{M}_{67}$ are as in Table 2. The lower sections give the corresponding information for the modulation at the orbital and half the orbital period for the Cerro Tololo infrared data.

Emission line	F	A_{67}	$\Delta\phi_{67}$	$\mathcal{M}_{67}$
a) Hubble Space Telescope:				
C III 1175	13 000	$11\,900 \pm 810$	+0.045	0.954
Ly α	27 300	$13\,000 \pm 1000$	+0.035	0.646
N V 1240	10 300	6990 ± 480	+0.005	0.807
Si III 1300	6190	7720 ± 260	+0.04	1.11
C II 1335	9400	4870 ± 390	+0.035	0.682
Si IV 1400	23 300	$17\,300 \pm 660$	+0.02	0.853
C IV 1550	56 400	$37\,500 \pm 1400$	+0.00	0.798
b) International Ultraviolet Explorer:				
Si IV 1400	21 300	$14\,100 \pm 1800$	+0.015	0.796
C IV 1550	51 600	$39\,400 \pm 3000$	+0.005	0.865
He II 1640	6740	8490 ± 980	+0.045	1.11
Al III 1860	4960	4560 ± 720	+0.030	0.958
c) ESO EFOSC2:				
He II 4686	1413	453 ± 58	+0.025	0.484
H β	11 288	5135 ± 350	+0.01	0.625
He I 5875	2288	1114 ± 73	−0.005	0.654
H α	10 113	3463 ± 238	+0.01	0.510
d) Cerro Tololo IRS:				
P δ	2060	412 ± 14	+0.020	0.333
P β	2080	334 ± 15	+0.020	0.277
B γ	585	8 ± 5	+0.000	0.026
Emission line	F	A_{98}	$\Delta\phi_{98}$	$\mathcal{M}_{98}$
P δ	2060	139 ± 17	+0.330	0.126
P β	2080	157 ± 17	+0.275	0.140
B γ	585	40 ± 8	+0.240	0.130
Emission line	F	A_{49}	$\Delta\phi_{49}$	$\mathcal{M}_{49}$
P δ	2060	48 ± 15	+0.025	0.045
P β	2080	100 ± 15	+0.015	0.092
B γ	585	30 ± 5	−0.025	0.098

about 3×10^{10} cm diameter centered on the location of the white dwarf, quite likely the accretion disk or ring filling about 80% of the Roche lobe. A shallow wide eclipse was also seen in the optical data of Siegel et al. (1989) in addition to the narrow eclipse of the accretion funnel. In our infrared data, the time resolution is not sufficient to disentangle the funnel and disk contributions to the eclipse. The central depth of the mean K-band eclipse is about 1.2×10^{-16} erg cm^{-2} s^{-1} Å^{-1} or 1.8 mJy.

The infrared emission lines display a different orbital modulation and a weaker eclipse. Figure 2 (lower right panel) shows $P\beta$ as an example. The light curve is practically flat in the interval $\phi_{98} = 0.5$–1.0 and shows a hump at $\phi_{98} = 0.25$ which is phase shifted with respect to the blue continuum hump (Hellier et al. 2000) by roughly 180°. The fit shown along with the data includes the 98-min and the 49-min variations which represent the first two terms of a Fourier expansion $\sum A_n \cos 2\pi\, n\, \phi_{98}$ of the orbital light curve. We interpret the maximum of the Paschen line flux as due to the inner illuminated side of the bulge, whereas the blue continuum originates from its outside heated by the interaction of the stream with the disk. This bulge is also detected by its ultraviolet line absorption (see Sect. 4.4 below).

3.3. Ellipsoidal modulation of the secondary star

In the infrared, the principal orbital modulation of the continuum is a double wave of 49 min period. There is no significant modulation at the orbital period. The minimum at $\phi_{98} = 0.98$ coincides with the center of the eclipse to within 0.01 in ϕ_{98}. Figure 2 (left lower panel) shows the variation of the K-band flux, with the other infrared bands behaving similarly. Table 2 lists the relevant fit parameters for our four infrared bands. The modulation depth is $\mathcal{M} = 0.13$ in K and decreases to 0.09 in the quasi-I band.

The double wave looks like the ellipsoidal modulation of the secondary star. While such a modulation is expected, studies of other CVs show that other light sources can mimic the ellipsoidal modulation. In the dwarf nova IP Peg, part of the double hump structure likely occurs in the accretion disk (Froning et al. 1999) and in the magnetic system AR UMa, beamed cyclotron emission may contribute (Howell et al. 2001). Model calculations of Kube et al. (2000) for magnetic CVs demonstrate that a double hump can also result from the accretion stream. Typically, however, the energy distributions of the additional light sources differ from that of the secondary star and phase-resolved spectrophotometry should be able to disentangle their contributions. E.g., in low-state spectrophotometry of the magnetic system UZ For, the ellipsoidal modulation in the near infrared can safely bex separated from the bluer cyclotron source (Schwope et al. 1990).

Considering these examples, we accept that some of the observed double hump modulation in EX Hya may originate from the accretion disk, but assume also that this contribution is less important than in other CVs as, e.g. IP Peg. The reason is that EX Hya displays no equivalent to the double hump in the optical continuum (Siegel et al. 1989; Hellier et al. 2000) nor in the optical and infrared emission lines. Also, the accretion disk in EX Hya is not well developed (King & Wynn 1999). Another effect which could affect the observed double humped light curve is the eclipse of the secondary star at superior conjunction ($\phi_{98} \simeq 0.48$) by the accretion disk. If the disk is largely optically thin, however, as suggested below, the magnitude of this obscuration would be small. In order to account for any other contribution to the 49-min infrared modulation in EX Hya, we take the amplitude of the ellipsoidal modulation to be $A_{\rm ell} = \alpha\, A_{49}$ with $\alpha \leq 1$, where $A_{\rm ell}$ is the amplitude of the ellipsoidal modulation at $\phi_{98} = 0.5$. In estimating α, we refer to the analysis of the ellipsoidal modulation in IP Peg by Froning et al. (1999) which yields $\alpha \simeq 0.5$. For the reasons given above, we expect that in EX Hya a larger fraction is of ellipsoidal origin and adopt $\alpha = 0.6 \ldots 1.0$ as a plausible range.

We determine the flux f of the secondary star from $A_{\rm ell}$ and an expression for the relative modulation $A_{\rm ell}/f$. To this end, we again refer to the numerical study of Froning et al. (1999) who carefully determined the modulation using the H-band gravity and limb darkening coefficients of a Roche lobe filling secondary star of $T_{\rm eff} = 3000\,$K, similar to that in EX Hya. Their result can be scaled as

$$A_{\rm ell}, H/f_H = 0.13\,\frac{\sin^2 i}{1+q}, \tag{2}$$

where f_H is the equivalent spectral flux of a spherical star, $q = M_2/M_1$ is the mass ratio, i is the orbital inclination, the functional form of Eq. (2) is that of the dominant term in Kopal's analytic expression (Binnendijk 1974), and the index H refers to the H-band. With $i = 79°$ (Hellier et al. 2000), $q \simeq 0.19 \pm 0.04$ (Hellier et al. 1987; Vande Putte et al. 2002), and $\alpha = 0.8 \pm 0.2$ we then have

$$f_H = 7.7\,\alpha A_{49,H}\,\frac{1+q}{\sin^2 i} = (7.6 \pm 2.0)\,A_{49,H} \tag{3}$$

where the error accounts for the uncertainties in α, $A_{49,H}$, and q. With $A_{49,H}$ from Table 2, we obtain the H-band flux of the secondary star in EX Hya as $f_H = (9.2 \pm 2.4) \times 10^{-16}\,{\rm erg\,cm^{-2}\ s^{-1}\ \AA^{-1}}$ or $8.0 \pm 2.1\,$mJy, where most of the error is systematic in nature and represents the full acceptable range, not a standard deviation. Using the numerical factor of Eq. (2) for all infrared bands, we obtain the fluxes plotted in Fig. 4 (open circles, statistical errors only). Because of the wavelength dependence of limb darkening (e.g. Al-Naimiy 1978), the true spectral energy distribution may be slightly redder (with a pivot point at H). This is consistent with the spectral distribution of the secondary star determined below (Sect. 4.3). Of the total orbital mean K-band flux of 13.3 mJy, this interpretation then assigns 7.3 mJy to the secondary star. Its infrared magnitude is $K = 12.43^{+0.24}_{-0.30}$. We continue the discussion of the spectrum of the secondary star in Sect. 4.3.

Of the remaining mean K-band flux, we attribute 1.2 mJy to the the accretion funnel and 4.8 mJy to the accretion disk and white dwarf (Sects. 4.2 and 4.4). Since about 1/2 of the funnel emission and about 1/5 of the disk are eclipsed, we expect a central depth of the partial eclipse of about 1.7 mJy or $1.1 \times 10^{-16}\,{\rm erg\,cm^{-2}\ s^{-1}\ \AA^{-1}}$, equal to the observed depth within the uncertainties (Sect. 3.2).

4. Spectral analysis

4.1. Overall spectrum

Figure 3 (upper left panel) shows the mean overall spectral energy distribution of EX Hya from the ultraviolet to the infrared. The mean IUE and HST spectra agree in absolute flux (Table 2) and, in the region of overlap, we show the less noisy HST spectrum. We have also schematically included the ORFEUS II continuum of Mauche (1999) which agrees reasonably well with the HUT spectrum of Greeley et al. (1997). In judging the overall spectrum, one should note that the individual sections were not observed contemporaneously. In spite of this, an astoundingly coherent view emerges. The spectrum clearly shows the Balmer, the Paschen, and the Brackett jumps in emission and, hence, contains substantial optically thin components, as suspected already by

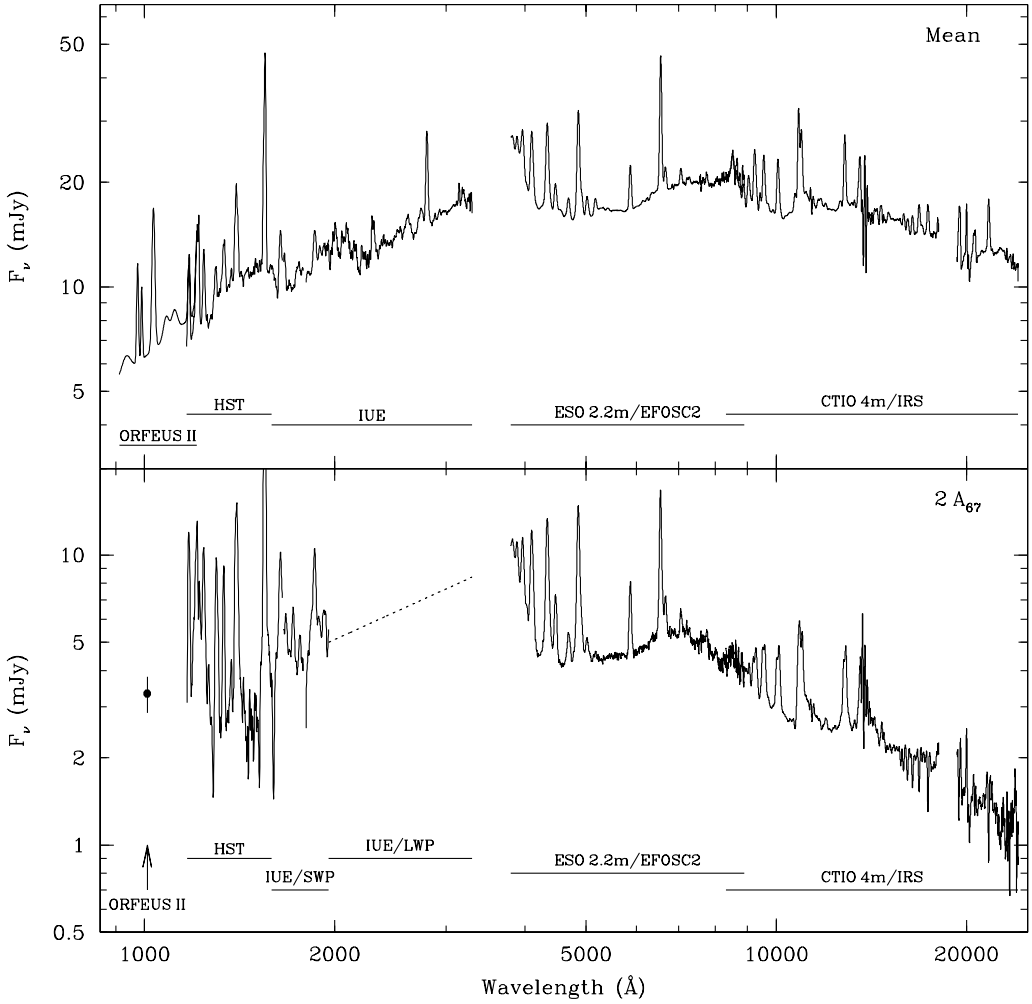

Fig. 3. *Top:* mean spectrum of EX Hya from 1000 to 24 000 Å. *Bottom:* difference between spin maximum and spin minimum spectra. See text for the long wavelength IUE part of the spectrum (dotted).

Berriman et al. (1985) on the basis of the infrared colours of EX Hya.

4.2. Spectrum of the spin-modulated component

The spin-modulated component has been extracted at all wavelengths and the amplitudes A_{67} of the broad bands and the line fluxes are listed in Tables 2 and 3. The difference between the spectral fluxes at spin maximum and spin minimum, $2\,A_{67}(\lambda)$, is depicted in the lower panel of Fig. 3. In the long-wavelength IUE range, the modulation amplitude could not be measured because of the lack of time resolution. We have, therefore, represented this spectral section schematically by the dotted line which has the mean slope of the long-wavelength spectrum and is adjusted to the modulated flux of the short wavelength IUE spectrum. The modulation of the ORFEUS II spectrum at 1010 Å (Mauche 1999) is indicated by a single data point. The spin-modulated component displays emission lines of the Balmer and Paschen series and the associated jumps in emission, while the Brackett lines appear in absorption (see above). The mean full base width of the ultraviolet emission lines corresponds to velocities of $\pm 2300\,\mathrm{km\,s^{-1}}$ (see Fig. 8, below), typical of the funnel at a couple of white dwarf radii.

Spin modulation originates from the rotating partially optically thick accretion funnels at both poles of the white dwarf. Because any optically thin and non-occulted component is constant in time, the mean funnel flux $f_{\rm fun}(\lambda) \geq A_{67}(\lambda)$. We need, therefore, an additional assumption to deduce $f_{\rm fun}(\lambda)$ from $A_{67}(\lambda)$. We note that the bright ultraviolet lines of CIII, CIV, SiIII, SiIV, and NV are strongly modulated (see $\mathcal{M}_{67}$ in Table 3). For definiteness, we refer to the 80% modulation of the strongest ultraviolet line, CIV λ1550, and assume that this line originates entirely in the funnel which is not unreasonable because, as shown below, CIV absorption is weak in the white dwarf spectrum. Adopting the modulation of CIV λ1550 as representative of $f_{\rm fun}(\lambda)$, we compute the mean funnel flux to a first-order approximation as

$$f_{\rm fun}(\lambda) = 1.5\,A_{67}(\lambda). \qquad (4)$$

In the optical continuum, the eclipsed flux at spin maximum slightly exceeds the spin modulated flux which suggests a similar factor. Nevertheless, there are clearly uncertainties in defining $f_{\rm fun}(\lambda)$ by a simple relation as in Eq. (4). We expect the ultraviolet emission of the heated polar caps of the white dwarf to display a spin modulation, too, and separation of the two spin-modulated components becomes non-trivial (see Sect. 4.5). On the other

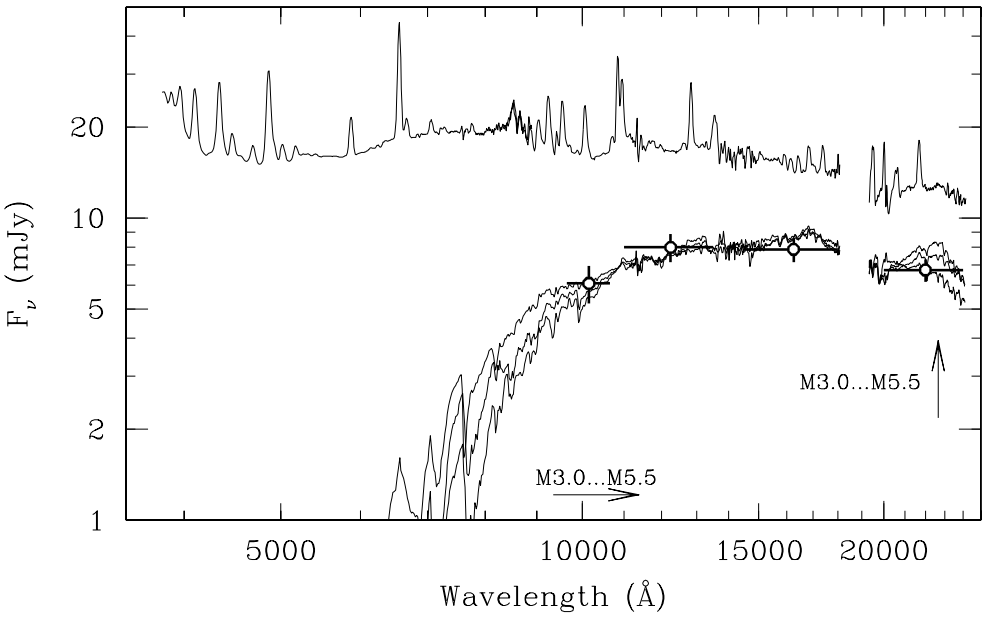

Fig. 4. Contribution of the secondary to the mean spectrum of EX Hya. The sample M-star spectra of spectral types M3.0, M4.5 and M5.5, respectively, have been scaled to the expected fluxes (crosses) derived from the ellipsoidal modulations listed in Table 2 (see text). For clarity, the noisy region between the J and H-bands has been smoothed.

hand, $f_{\rm fun}(\lambda)$ clearly becomes small at long wavelengths and the implied error in the unmodulated component becomes then small, too. We use Eq. (4) to compute the contribution of the funnel emission to the luminosity, but do not attempt to model its spectral distribution.

4.3. Spectrum of the secondary star

Figure 4 shows the quasi-Johnson *IJHK* fluxes of the secondary star as defined above (Sect. 3.2.2.) along with the spectra of M3 to M5.5 stars least squares fitted to the data points for $\alpha = 0.8$. The systematic uncertainty in the flux is at most 2 mJy (Sect. 3.3).

Formally, the four data points are best fitted by an M3 star, but, as noted above, the true spectrum will be slightly redder and the spectral type later, about M3 to M5, still consistent with the M3 assignment by Dhillon et al. (1997). The contribution of the secondary star to the total spectrum is largest at long wavelengths and the only pronounced distinctive feature in this range is the broad hump which is centered at $\sim$2.2 μm and flanked by H_2O absorption dips. This feature is clearly visible also in the spectrum of EX Hya. We determine the most probable contribution from the secondary star by subtracting the spectrum of an M3, an M4.5, and an M5.5 star from the observed spectrum. Figure 5 shows the corresponding difference spectra. We expect this spectrum to decrease smoothly since the main contributions should be from the spin-modulated component (Fig. 3) and the accretion disk (Fig. 7) and both decrease with wavelength. The smoothest decrease is obtained for the M4.5 star, in agreement with the expected spectral type in a CV with 98 min orbital period (Beuermann et al. 1998). We adopt a spectral type M4 $\pm$ 1.

The detection of absorption lines from the secondary in EX Hya is difficult. Figure 6 compares the spectrum of the M4.5 dwarf Gl 285 with spectra of EX Hya collected near spin minimum: (i) mean spin minimum, (ii) ellipsoidal maximum ($\phi_{98} \simeq 0.75$) near spin minimum, and (iii) eclipse ($\phi_{98} \simeq 0$, backside of star) near spin minimum. The M-star features are largely obscured by lthe emission line components in the 8300–9600 Å range. In the K-band, the presence of the M-star is indicated by the faint NaI doublet and the CO molecular bands (see also Dhillon et al. 1997). Although our spectral resolution is not sufficient to resolve the NaI lines, phase-shifted superposition of the spectra suggests that NaI absorption is preferentially present on the dark side of the star and displays a radial velocity consistent with the motion of the secondary star (an uncertain 400 km s^{-1}). Higher resolution is needed to settle the question of the radial velocity of the secondary star (Vande Putte et al. 2002).

4.4. Spectrum of the accretion disk

Figure 7 shows the (slightly smoothed) spectrum which remains after subtraction of the funnel component $f_{\rm fun}(\lambda)$ and the secondary star, assuming it has $K = 12.43$, and is a dM4.5 star (Figs. 4 and 5). We assign this spectrum to the sum of the accretion disk including the bright spot at its edge and the white dwarf. The spectrum lacks the intense ultraviolet lines which belong to the funnel component, but contains a substantial fraction of the HeI, Balmer, Paschen, and Brackett line emission. MgII λ2800 may, in part, originate in the funnel and be falsely assigned to the disk because we subtracted the long-wavelength IUE contribution to the funnel spectrum only in a schematic way without accounting for the emission lines. The (unsmoothed) short-wavelength section of the spectrum in Fig. 7 is shown enlarged in the insert and is further discussed in Sect. 4.5 (Fig. 9). This part of the spectrum is dominated by the heated white dwarf.

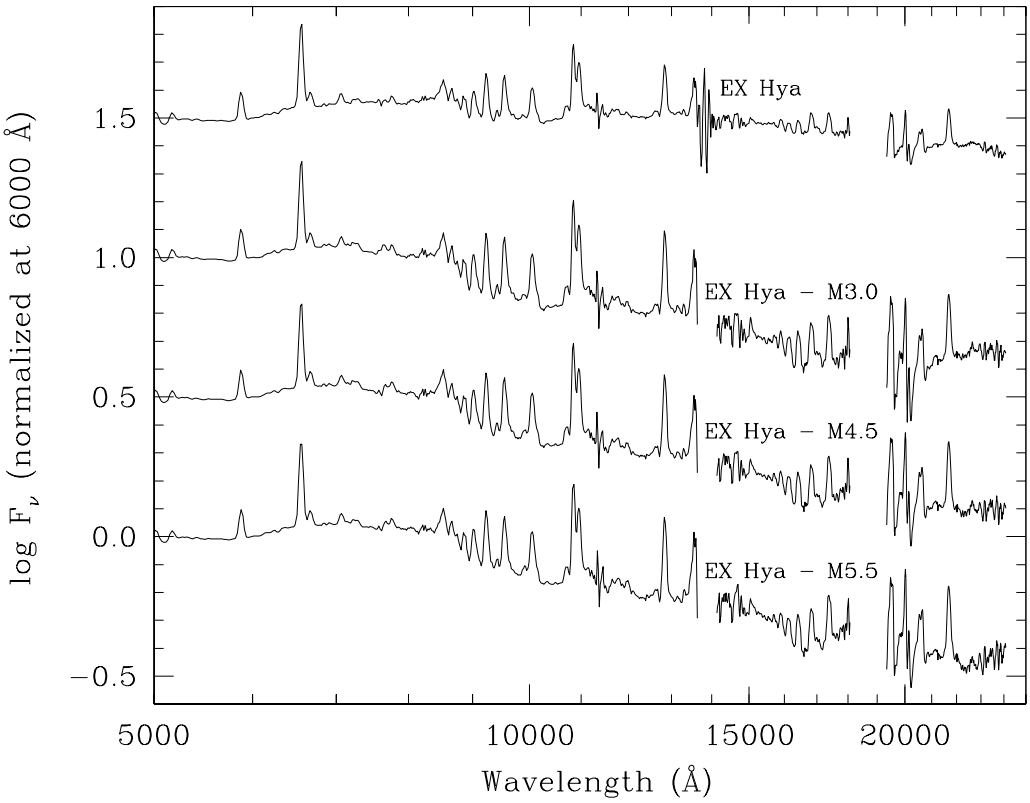

Fig. 5. Mean spectrum of EX Hya (top) with the scaled sample M-star spectra from Fig. 4 subtracted. The individual spectra have been offset by multiples of 0.5 flux units for clarity.

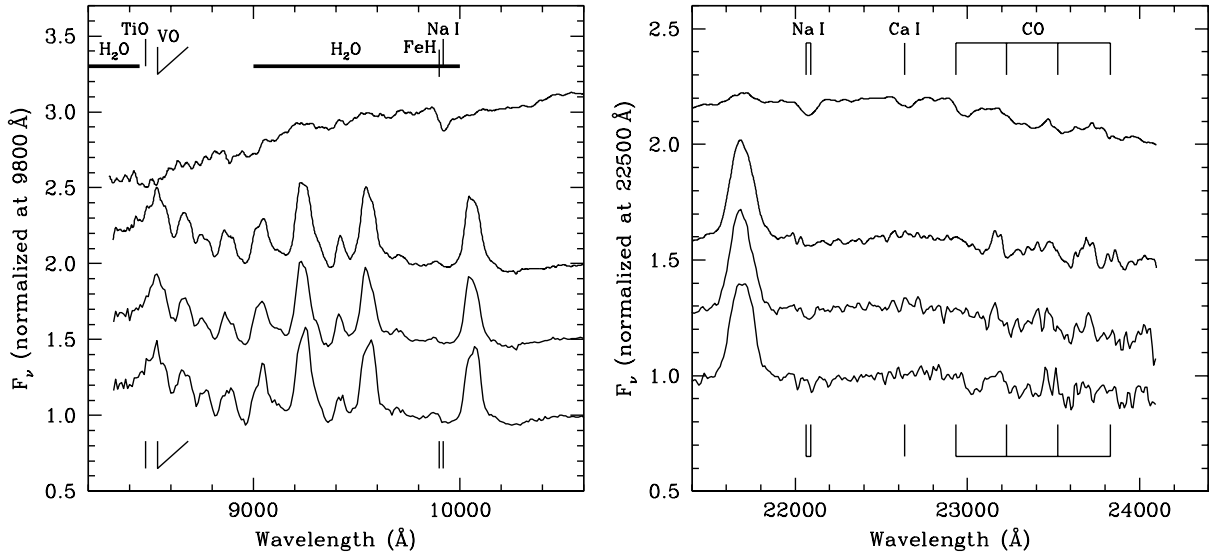

Fig. 6. Spectral signatures of the secondary star in the IR spectrum of EX Hya. Both panels show the spectrum of the M4.5 star Gl285 and three spectra of EX Hya, (i) mean near spin minimum, (ii) 49-min maximum near spin minimum, and (iii) eclipse near spin minimum (from top to bottom). All spectra are normalised to unity at 9800 Å (left panel) or 22 500 Å (right panel) and vertically offset by multiples of 0.5 flux units (left panel) and 0.3 flux units (right panel). Spectral features expected to be present in the secondary star are indicated. H_2O refers to regions affected by atmospheric water vapour absorption. The strong emission lines in the EX Hya spectra are the hydrogen Paschen series and CaIIλ8498, 8542, 8662 (left panel) and Bγ (right panel).

We model the $\lambda > 3000$ Å part of the spectrum by an isobaric and isothermal disk of pure hydrogen plus a blackbody representation of the white dwarf. The spectrum of the disk is computed following the description of Gänsicke et al. (1997). It has an outer radius of 1.6×10^{10} cm, a thickness of 2×10^8 cm, a pressure of 200 dyne cm^{-2}, an electron temperature of 7000 K, close to the canonical temperature of an optically thin accretion

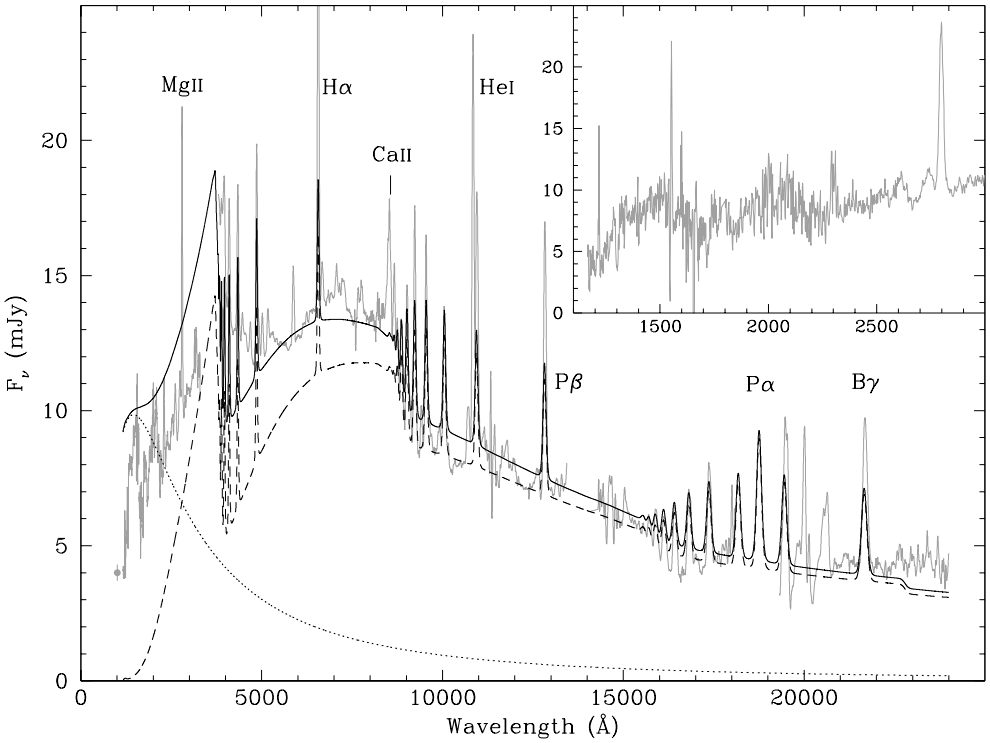

Fig. 7. Slightly smoothed spectrum of EX Hya after subtraction of the spin-modulated funnel component and the secondary star. A single data point at 1010 Å denotes the unmodulated flux of the ORFEUS spectrum (Mauche 1999). Also shown are the model spectrum of the accretion disk (dashed curve), a schematic representation of the white dwarf (dotted curve), and the sum (solid curve). The insert shows an expanded version of the unsmoothed ultraviolet part of the spectrum.

disk (Williams 1980), and is seen at an inclination of 79°. For definiteness, we assume that the disk has a central hole of 6×10^9 cm radius (Hellier et al. 1987), but the structure could also be a ring with a larger inner radius surrounding the magnetosphere of the white dwarf. This component is optically thin and accounts for much of the line emission and the Balmer, Paschen, and Brackett jumps, but lacks continuum flux around 5000 Å. We include, therefore, a second component which has a pressure of 10^3 dyne cm^{-2}, an electron temperature of 10 000 K, a weak Balmer jump, and is nearly optically thick. The hotter component covers only ∼20% of the area of the cool one and may represent the heated inner edge of the disk (but see Sect. 4.5). Figure 7 shows the sum of the two disk components (short-dashed curve). Although this is not a formal fit, it reproduces the observed optical and infrared part of the spectrum reasonably well. Metal line emission (mostly FeII, not included in the model) may substantially contribute to the observed excess in the range 4000...5500 Å. Lines of the Pfund series (not included either) may contribute to the excess flux longward of 22 788 Å.

The spectrum in Fig. 7 is based on $K = 12.43$ for the secondary star. If the secondary were substantially brighter, the decreased infrared flux could not be fit by the optically thin spectrum anymore; if it were fainter, there could be additional disk flux over that depicted in Fig. 7 within the limits set in Sect. 3.3. The 2 mJy uncertainty in the K-band flux of the secondary, would allow an underlying cool component of the disk with a blackbody temperature up to $T_{\rm bb} = 3300$ K for a disk radius of 1.6×10^{10} cm. This is a significant result because the mass in the modeled disk is $\lesssim 6 \times 10^{19}$ g, much less than the $\sim 10^{22}$ g needed to feed one of the rare outbursts. If the outbursts result from a disk instability, a layered disk is needed in which the component of high surface density must be cooler than the limit given above. This result is very similar to the conclusions of Gänsicke et al. (1997) for the case of the SU UMa dwarf nova EK Tra.

Figure 8 shows the HST spectrum before and after eclipse, at $P_{\rm orb} = \pm(0.05$–$0.15)$. Before eclipse pronounced selfabsorption cores of highly excited ultraviolet lines are seen which disappear after the eclipse. These cores are produced in the bulge at the edge of the accretion disk, i.e. the interaction region of the accretion stream with the disk or ring. This bulge produces also the enhanced Paschen line emission at $\phi_{98} = 0.25$, the orbital maximum in the B-band at $\phi_{98} = 0.85$ (Hellier et al. 2000), and the pre-eclipse dip in the EUV and soft X-ray regime (Córdova et al. 1985; Rosen et al. 1988; Hurwitz et al. 1997; Mauche 1999). The radial velocity of the absorption lines in the difference spectrum (C in Fig. 8) is consistent with zero, as expected for material at the edge of the disk or ring which moves essentially perpendicular to the line of sight. The presence of NV indicates an excitation temperature of the order of 50 000 K or higher. The metal lines are just resolved with a $FWHM$ of 2.5 Å, corresponding to about 400 km s^{-1}. The Lyα absorption line in the difference spectrum is wider with $FWHM \simeq 5$ Å (1000 km s^{-1}), suggesting an origin in warm material or material with a large velocity dispersion. The column density needed to produce the bulge absorption in Lyα at $\phi_{98} \sim 0.9$ is about 10^{19} H-atoms cm^{-2}, substantially less than the equivalent column density of 1.3×10^{20} H-atoms cm^{-2} of cold matter of solar composition needed to account for the observed

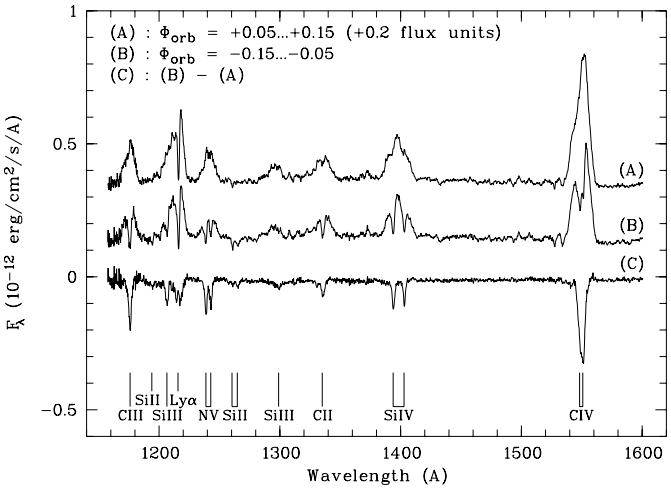

Fig. 8. Spin averaged HST spectra of EX Hya before and after eclipse ($\phi_{98} = -0.15...-0.05$ and $\phi_{98} = +0.05...+0.15$, upper two spectra) and difference spectrum (bottom). The identifications of the narrow absorption lines are indicated (see text).

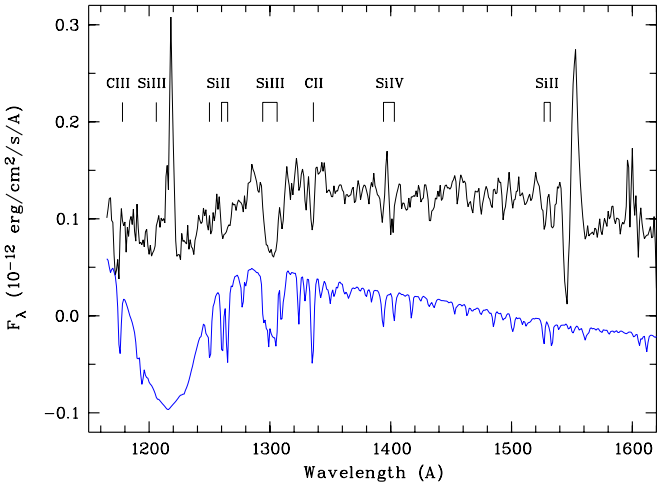

Fig. 9. HST spectrum of EX Hya with the funnel component removed. The extension for $\lambda > 1590$ Å is from the IUE spectrum. A 25 000 K white dwarf spectrum with solar composition is shown for comparison (offset by −0.1 units).

EUV bulge absorption (Hurwitz et al. 1997). The difference suggests that hydrogen is largely ionized and the EUV bulge absorption is primarily due to helium.

4.5. Spectrum of the white dwarf

The ultraviolet section of the spectrum in Fig. 7 is reproduced in Fig. 9. It shows the typical absorption lines expected from a hot atmosphere, including CIII λ1175, SiII λ1260, 1265, SiII,III λ1294 ... 1306, CII λ1335, SiIV λ1394, 1403, and SiII λ1527, 1533. Some of the lines are affected by the subtraction procedure by which this spectrum was created, CIV λ1550, SiIV λ1394, 1403, and probably CIII λ1175. In order to estimate the temperature of the white dwarf (or its heated pole cap) in EX Hya, we have computed a set of white dwarf spectra covering $T_{\rm eff}$ = 15 000–50 000 K in steps of 5000 K, using the codes TLUSTY 195 and SYNSPEC 45 (Hubeny 1988; Hubeny & Lanz 1995), assuming solar abundances and $\log g = 8.0$ (i.e. $M_\odot \simeq 0.6$). The observed line ratios SiIII/SiII and CIII/CII constrain the temperature of the white dwarf photosphere to $T_{\rm eff} = 25\,000 \pm 3000$ K and a white dwarf model of this temperature qualitatively fits also the absorption lines of other heavy elements. For an distance of 65 pc (Sect. 5.2), the observed flux in the range 1300–1500 Å corresponds to a white dwarf radius of 6×10^8 cm.

We do not attempt a detailed fit to the white dwarf spectrum for the following reasons: (i) the irradiated white dwarf has very likely a non-uniform temperature distribution; (ii) the spectrum is probably altered by attenuation in the accretion curtain; and (iii) the long wavelength part of the white dwarf spectrum is heavily veiled by the accretion disk and practically unobservable. We comment on these points in turn.

The funnel radiation which impinges on the white dwarf will produce extended hot polar caps. Taking account of these effects would introduce additional parameters which are not well constrained. Furthermore, heating affects the temperature structure of the white dwarf atmosphere and thereby alters the profiles of the absorption lines. In the polar AM Her, where the FUV emission is dominated by emission from the white dwarf, we could show that irradiation results in a significantly decreased depth of the Lyα absorption line (Gänsicke et al. 1998). A similar effect could explain the shallow Lyα absorption observed in EX HYa.

The mean photospheric spectrum of the white dwarf is probably altered by the fact that part of the light is attenuated on its passage through the accretion curtain. An indication for this is provided by the double hump structure of the spectrum shown in the insert in Fig. 7. Such spectral shape is reminiscent of the white dwarf spectrum in OY Car which is heavily veiled by metal absorption in material referred to as "FeII curtain" (Horne et al. 1994). There is, in fact, a detailed similarity between the ultraviolet spectrum in Fig. 7 and that of the white dwarf in OY Car (Fig. 5, bottom panel of Horne et al.). Metal absorption in the funnel produces the broad dips around 1700 Å and 2500 Å, and the remnant spike at 1595 Å. Given that funnel emission and absorption is abundant at other wavelengths, we are not surprised to find funnel absorption features mixed up with photospheric ones. The strong absorption lines indicated in Fig. 9 are not noticeably broadened, however, and probably of photospheric origin.

If part of the ultraviolet emission is due to a white dwarf with heated polar caps, we may expect that the flux shows spin-modulation. There are spin-modulated contributions to the ultraviolet flux by the accretion funnel *and* by the heated white dwarf. The best visibility of the accretion funnel is when the lower pole points towards the

observer (Beuermann & Osborne 1988). At this rotation phase, $\phi_{67} = 0$, the heated polar caps reach their minimum projected area. Hence, the spin modulated component from the heated polar caps assumes its minimum when the funnel flux reaches its maximum, i.e., the two modulations will be out of phase by 180°. The amplitude of the spin modulation will then display a minimum near 1500 Å, where the spectral flux of the white dwarf reaches a maximum, as it is observed (Fig. 3).

Finally, there will be a contribution from the unheated fraction of the white dwarf photosphere. For an effective temperature of 10 000–15 000 K and 10^9 cm radius, the peak flux would reach only 1–3 mJy and can not be identified against the other components. It might be contained, e.g., in the adopted disk flux which would then have to be reduced correspondingly (Sect. 5.4).

5. System parameters

5.1. Mass and radius of the secondary star

We assume that the secondary is a main sequence star which is negligibly expanded over its zero age main sequence radius (Baraffe et al. 1998; Kolb & Baraffe 1999; see also Beuermann et al. 1998). For stars of solar composition, the Baraffe et al. mass radius relation of spherical stars may be approximated by a power law of the type $R \propto M^{\beta}$ for limited ranges of mass. Considering that the equilibrium radius of a Roche lobe filling star of the same mass is larger by about 6% (Kolb 2001), we obtain

$$R_2/R_\odot = 0.77\,(M_2/M_\odot)^{0.75} \tag{5}$$

for masses between 0.11 and $0.40\,M_\odot$. The relation of Patterson (1984), $R_2/R_\odot = (M_2/M_\odot)^{0.88}$, predicts radii within 5% of this for masses between 0.09 and $0.20\,M_\odot$. Eq. (5) and Roche geometry yield $M_2 = 0.12 \pm 0.01\,M_\odot$ and $R_2 = (0.157 \pm 0.010)\,R_\odot = (1.09 \pm 0.07) \times 10^{10}$ cm, where we have allowed for some systematic error in M_1. If the mass exceeds $0.13\,M_\odot$, the secondary would have to be smaller than a main sequence star. If it is as low as $0.10\,M_\odot$, an expansion in radius by more than 10% would be required.

5.2. Distance of EX Hydrae

The detection of the secondary star in EX Hya allows to obtain an estimate of the distance d by the surface brightness method (Bailey 1981),

$$\log d = (K - S_K)/5 + 1 + \log\,(R/R_\odot). \tag{6}$$

We use the re-calibration of the K-band surface brightness of late type stars by Beuermann (2000) which yields $S_K = 4.37 \pm 0.22$ for a dwarf of spectral type M3–5 and near-solar composition. With $K = 12.19 \ldots 12.73$ and the stellar radius of the last section, we obtain a distance $d = 65 \pm 11$ pc. This is much lower than previous estimates which include 105 pc (Warner 1987) and >130 pc (Berriman et al. 1985). EX Hya may be one of the closest CVs with a known distance.

The largest contribution to the error in d arises from the uncertainty in the K-magnitude of the secondary (Sect. 3.3). The distance is near the upper limit of the derived range if the true ellipsoidal modulation is as small as 60% of the observed 49-min variation. Because of this uncertainty and the special importance of EX Hya among all CVs, a trigonometric parallax for this object is needed.

5.3. Interstellar absorption

X-ray spectral fits suggest that the X-ray source is partially covered by substantial column densities $N_{\rm H}$ of hydrogen (e.g. Allan et al. 1998). This is material within the binary system. The detection of EUV emission (Hurwitz et al. 1997) proves that the true interstellar column density is small. Fitting the narrow Lyα-absorption profile in the $\phi_{98} = 0.05$–0.15 spectrum of Fig. 8 yields $N_{\rm H} \simeq (3 \pm 1) \times 10^{18}$ H-atoms cm^{-2}, consistent with the non-detectable extinction, $E_{B-V} \lesssim 0.05$ (Verbunt 1987). At $d = 65$ pc, the mean space density of neutral atomic hydrogen along the line of sight to EX Hya $(l, b = 304°, +33°)$ is $n_{\rm H} = 0.01 \ldots 0.02$ cm^{-3}.

5.4. Luminosity

We estimate the luminosity as $L = 4\,\pi\,d^2\,F$, where F is the orbital and spin-averaged energy flux, with the secondary star subtracted and corrected for interstellar absorption using $N_{\rm H} = 3 \times 10^{18}$ H-atoms cm^{-2} of cold matter. There is some uncertainty in the estimate of L because the mean flux used may deviate from the 4π-average.

Table 4 lists the mean fluxes in individual energy bands shortward of Lyα and for individual physical components longward of Lyα. The mean X-ray flux is collected from Beuermann & Osborne (1984); Córdova et al. (1985); Rosen et al. (1988); Rosen et al. (1991), Singh & Swank (1993) and Allan et al. (1998). The observed EUV and soft X-ray flux in the 0.067–0.280 keV range is $\sim 0.7 \times 10^{-11}$ erg cm^{-2} s^{-1} (Córdova et al. 1985; Hurwitz et al. 1997) which after correction for interstellar absorption increases to $\sim 10^{-11}$ erg cm^{-2} s^{-1}. There is no information on the flux between 13.6 and 67 eV and we simply add another $\sim 10^{-11}$ erg cm^{-2} s^{-1}.

Angle-dependent absorption and scattering in the funnel is probably responsible for the observed low-energy depression and the spin modulation of the EUV and X-ray spectrum (e.g. Kim & Beuermann 1995). The flux contained in the spin-modulated soft and hard X-ray components, i.e. half the difference between maximum and minimum fluxes for photon energies >0.28 keV, amounts to 3×10^{-11} erg cm^{-2} s^{-1}. Applying the Zanstra method to the flux in the HeIIλ4686 line, $F_{4686} = 1.65 \times 10^{-13}$ erg cm^{-2} s^{-1} (Patterson & Raymond 1985, this work), demonstrates that an additional flux $F_{>54} \simeq 3 \times 10^{-11}$ erg cm^{-2} s^{-1} is absorbed at photon energies

Table 4. Energy fluxes of the spectral components of EX Hya.

Component	E (keV) or λ (Å)	Flux (10^{-11} erg cm^{-2} s^{-1})
Hard X-rays	≥1.0 keV	15
Soft X-rays	0.28...1.0 keV	3
EUV	0.067...0.28 keV	∼1
	0.0136...0.067 keV	∼1:
Accretion curtain	$\lambda = 912...24\,000$ Å	12
Accretion disk	$\lambda = 912...24\,000$ Å	10
White dwarf	$\lambda = 912...24\,000$ Å	18
Total		60

between 0.054 and 0.28 keV. The sum of these two components is the minimum reprocessed flux expected from the accretion funnel. The funnel emission will actually be higher because additional energy is absorbed from the Lyα continuum below 54 eV and from the Balmer continuum of the heated white dwarf. Furthermore, viscous interaction of the accreted gas in the funnel may release additional energy. The sum of all these sources should account for the mean observed funnel emission of 12×10^{-11} erg cm^{-2} s^{-1} which appears reasonable. The latter number is the wavelength-integral of the funnel component for $\lambda > 912$ Å , $F_{\rm fun} = 1.5 \int A_{67}\,{\rm d}\lambda$ (see Sect. 3.1 and Fig. 3).

Subtracting the funnel component and the secondary star from the mean spectrum leaves the accretion disk and the white dwarf (Fig. 7). In Table 4, the disk is represented by the integral over the dotted spectrum in Fig. 7 and the white dwarf by the flux remaining after subtraction of the dotted spectrum. The disk component contains about 1/6 of the total flux (Table 4) a bit more than expected from gravitational energy release outside $r_{\rm i} \simeq 6 \times 10^9$ cm and a white dwarf of radius $R_1 = 10^9$ cm. Note that this result does not allow an inner disk radius $r_{\rm i} < 6\,R_1$, consistent with the visibility of the lower pole of the white dwarf in X-rays (Beuermann & Osborne 1988).

The intrinsic flux of the white dwarf can not be separately identified and is included in the contribution quoted for either the heated white dwarf or the accretion disk (Table 4). For $R_1 = 10^9$ cm and an effective temperature of the white dwarf of 10 000–15 000 K, it amounts to only $(2-6) \times 10^{-11}$ erg cm^{-2} s^{-1}. Hence, the total accretion-induced flux is slighly reduced below the sum of the fluxes in Table 4 to about 5.6×10^{-10} erg cm^{-2} s^{-1}. This corresponds to a luminosity of $L = 2.8 \times 10^{32}$ erg s^{-1} at $d = 65$ pc, or $L = 6.7 \times 10^{32}\,d_{100}^2$ erg s^{-1}, where d_{100} is the distance in units of 100 pc. Not included in Table 4 is the secondary star which contributes only 1.5×10^{-11} erg cm^{-2} s^{-1}.

5.5. Accretion rate

The accretion rate is obtained as $\dot{M} = L\,R_1/GM_1$, where M_1 and R_1 are mass and radius of the white dwarf. With L from the last section, $\dot{M} = 5 \times 10^{15}(R_1/10^9\,{\rm cm})(M_1/M_\odot)^{-1}\,d_{100}^2\,{\rm g\,s^{-1}}$. M_1 is estimated from the X-ray temperature as 0.45–0.48 $M_\odot$ (Fugimoto & Ishida 1997; Cropper et al. 1999; Ezuka & Ishida 1999; Ramsay 2000). The radial velocity amplitudes of the white dwarf, $K_1 \simeq 69 \pm 9\,{\rm km\,s^{-1}}$ (Hellier et al. 1987), and of the secondary star, $K_2 \simeq 356 \pm 44\,{\rm km\,s^{-1}}$ (Vande Putte et al. 2002), yield $M_2 = 0.095\,M_\odot$ and $M_1 = 0.49\,M_\odot$. According to our discussion in Sect. 5.1, the secondary would have to be substantially expanded over a main sequence star if of such a low mass and we prefer the higher mass of $0.12\,M_\odot$ because, within the errors, K_1 and K_2 are consistent also with $M_2 = 0.12\,M_\odot$ and M_1 as high as $0.7\,M_\odot$. Given the remaining uncertainty in the masses, we quote the accretion rate in terms of a standard white dwarf of $0.6\,M_\odot$. Using a Wood (1994) white dwarf model with thick hydrogen envelope and $T_{\rm eff} = 10^4$ K, the radius is then $R_1 = 8.9 \times 10^8$ cm and $\dot{M} \simeq 7.5 \times 10^{15}\,d_{100}^2\,{\rm g\,s^{-1}}$ or $\dot{M} \simeq 3.1 \times 10^{15}\,{\rm g\,s^{-1}}$ at $d = 65$ pc. This is consistent with the accretion rate as expected from gravitational radiation as the dominant angular momentum loss mechanism. It is also consistent with the distance-independent accretion rate deduced from the observed spin-up rate of the white dwarf in EX Hya, $\dot{M}_{\rm spin} = 2.4 \times 10^{15}\,(r_{\rm i}/10^{10}\,{\rm cm})^{-1/2}\,{\rm g\,s^{-1}}$ for $M_1 = 0.6\,M_\odot$ (Ritter 1985) which is derived on the assumption that the accreted matter couples onto the magnetic field of the white dwarf at the inner disk radius $r_{\rm i}$. The estimated $r_{\rm i} \simeq 6 \times 10^9$ cm (Hellier et al. 1987) yields $\dot{M}_{\rm spin} \simeq 3.1 \times 10^{15}\,{\rm g\,s^{-1}}$. These numbers do not change substantially if $M_1 \simeq 0.5\,M_\odot$.

5.6. Magnetic field strength of the white dwarf

A coarse estimate of the (di–)polar field strength of the white dwarf of $B_{\rm p} \simeq 0.18$ MG can be derived from $r_{\rm i} \simeq 6 \times 10^9$ cm (Hellier et al. 1987) and $\dot{M} \simeq 3 \times 10^{15}\,{\rm g\,s^{-1}}$ if $r_{\rm i}$ is equated to $r_\mu \simeq 2^{-10/7}\mu^{4/7}(GM_1)^{-1/7}\dot{M}^{-2/7}$ cm, i.e. about 1/2 of the spherical Alfvén radius (e.g. Frank et al. 1992, their Eq. (6.12)). Larger $r_{\rm i}$ (Hellier et al. 2000) would lower the field estimate. Such a low field is consistent with the lack of cyclotron emission in the infrared.

6. Conclusions

We have detected the dM4 ± 1 secondary star in EX Hya by its ellipsoidal modulation and spectral energy distribution. From its infrared magnitude $K \simeq 12.5$, we have derived a distance of EX Hya of 65 ± 11 pc, substantially less than previous estimates. The integrated flux from the X-ray to the infrared range averaged over spin and orbital period is 6×10^{-10} erg cm^{-2} s^{-1}, yielding a luminosity of about 3×10^{32} erg s^{-1} and an accretion rate which is consistent with the observed spin-up and with gravitational radiation as the dominant angular momentum loss mechanism. Distance, luminosity, and accretion rate depend upon which fraction of the observed infrared continuum modulation at half the orbital period may be interpreted as ellipsoidal modulation of the secondary star.

If this fraction is near unity, d is near the lower limit of 55 pc, if it less than 60%, d may exceed 75 pc. This question can best be resolved by obtaining a trigonometric parallax.

The heated white dwarf is detected for the first time by strong metal absorption lines which are probably of photospheric origin, but may be affected also by absorption in the accretion funnel. The equivalent width ratios of the Si II, III, IV and C II, III lines suggest a near-solar metal abundance in the uppermost photospheric layers and an effective temperature near 25 000 K. The radius needed to account for the emission is about 6×10^8 cm. If the white dwarf is of low mass as suggested by several studies and has a radius of about 10^9 cm then what we see are probably the heated polar caps of the white dwarf. Intrinsically, the white dwarf may be substantially cooler than indicated by the line ratios (and perhaps display a less metal-rich surface composition). The observed "white dwarf flux" corresponds to ∼28% of the total accretion flux, consistent with the reprocessed fraction of the downward flux from the post-shock region considering both, geometry and reflection probability.

There is agreement that maximum light at optical and X-ray wavelengths occurs when the upper pole points away from the observer (Hellier et al. 1987; Beuermann & Osborne 1988; Rosen et al. 1988; Siegel et al. 1989; Hellier et al. 2000). At this spin phase, the light from the heated caps is likely to reach a minimum which implies antiphased modulations of the ultraviolet light from the funnel and the white dwarf surface. The minimum in the amplitude of the spin modulation near 1500 Å is consistent with this notation. More extensive ultraviolet observations can possibly disentangle the contributions from both components.

Of the outward directed integrated X-ray flux, the spin-modulated fraction of ∼20% is absorbed and reprocessed in the accretion funnel. The funnel spectrum is largely the result of radiative transfer of the X-ray emission from the accretion column and of the ultraviolet emission from the heated white dwarf. Although it is clear that the funnel is optically thick in the emission lines and partly in the continuum, the detailed funnel geometry remains uncertain and we have not attempted to model the resulting spectrum (Fig. 7). Better spectral resolution in the optical and infrared is needed to study the radiative transfer in detail.

The emission which is left after subtraction of the secondary star, the white dwarf, and the funnel emission originates from the accretion disk or ring surrounding the white dwarf magnetosphere. The spectral flux contribution of much of the remaining optical and infrared light is plausibly explained by an isothermal slab of gas of radius 1.6×10^{10} cm, thickness 2×10^8 cm, and a temperature of most of the gas near 7000 K which is optically thin plus a largely optically thick component at 10 000 K which covers only 20% of the emitting area of the disk. There is a tight upper limit on the blackbody temperature of an underlying optically thick component covering the entire disk of $T_{\rm bb} < 3300$ K.

In summary, we have presented an interpretation of the overall spectral energy distribution of EX Hya which explains the individual components within the standard model of a weakly magnetic intermediate polar.

Acknowledgements. We thank Dave Vande Putte and Robert Smith for making their K_2-measurement of EX Hya available to us prior to publication and Ivan Hubeny for providing recent versions of TLUSTY and SYNSPEC. This work was supported in part by BMBF/DLR grants 50 OR 9610 4 and 50 OR 9903 6.

References

Al-Naimiy, H. M. 1978, Ap&SS, 53, 181
Allan, A., Hellier, C., & Beardmore, A. 1998, MNRAS, 295, 167
Baraffe, I., Chabrier, G., Allard, F., & Hauschildt, P. 1998, A&A, 337, 403
Bailey, J. 1981, MNRAS, 197, 31
Beuermann, K. 2000, New Astr. Rev., 44, 93
Beuermann, K., & Osborne, J. P. 1984, Proc. X-ray Astronomy '84 (Bologna), ed. M. Oda, & R. Giacconi, 23
Beuermann, K., & Osborne, J. P. 1985, Space Sci. Rev., 40, 117
Beuermann, K., & Osborne, J. P. 1988, A&A, 189, 128
Beuermann, K., Baraffe, I., Kolb, U., & Weichhold, M. 1998, A&A, 339, 518
Berriman, G., Szkody, P., & Capps, R. W. 1985, MNRAS, 217, 327
Binnendijk, L. 1974, Vistas Astron., 16, 61
Córdova, F. A., Mason, K. O., & Kahn, S. M. 1985, MNRAS, 212, 447
Cropper, M. S., Wu, K., Ramsay, G., & Kocabiyik, A. 1999, MNRAS, 306, 684
Dhillon, V. S., Marsh, T. R., Duck, S. R., & Rosen, S. R. 1997, MNRAS, 285, 95
Depoy, D. L., Gregory, B., Elias, J., et al. 1990, PASP, 102, 1433
Ezuka, H., & Ishida, M. 1999, ApJS, 120, 277
Frank, J., King, A. R., & Raine, D. 1992, Accretion Power in Astrophysics (Cambridge Astrophys. Ser.), 2nd edition
Froning, S. S., Robinson, E. L., Welsh, W. F., & Wood, J. 1999, ApJ, 523, 399
Fugimoto, R., & Ishida, M. 1997, ApJ, 474, 774
Gänsicke, B. T., Beuermann, K., & Thomas, H.-C. 1997, MNRAS, 283, 388
Gänsicke, B. T., Hoard, D. W., Beuermann, K., Sion, E. M., & Szkody, P. 1998, A&A, 338, 933
Greeley, B. W., Blair, W. P., Long, K. S., & Knigge, C. 1997, ApJ, 488, 419
Hellier, C., Mason, K. O., Rosen, S. R., & Córdova, F. A. 1987, MNRAS, 228, 463
Hellier, C., & Sproats, L. N. 1992, IBVS, 3724
Hellier, C., Kemp, J., Naylor, T., et al. 2000, MNRAS, 313, 703
Horne, K., Marsh, T. R., Cheng, F. H., Hubeny, I., & Lanz, Th. 1994, ApJ, 426, 294
Howell, S. B., Gelino, D. M., & Harrison, T. 2001, AJ, 121, 482
Hubeny, I. 1988, Comput. Phys. Comm., 52, 103
Hubeny, I., & Lanz, T. 1995, ApJ, 439, 875
Hurwitz, M., Sirk, M., Bowyer, S., & Yuan-Kuen, K. 1997, ApJ, 477, 390
Kim, Y., & Beuermann, K. 1995, A&A, 298, 165

King, A. R., & Wynn, G. A. 1999, MNRAS, 310, 203
Kolb, U. 2001, Talk at the Göttingen Conf., ASP Conf. Ser., in preparation
Kolb, U., & Baraffe, I. 1999, MNRAS, 309, 1034
Kube, J., Gänsicke, B. T., & Beuermann, K. 2000, A&A, 356, 490
Kraft, R. P. 1962, ApJ, 135, 408
Kruszewski, A., Mewe, R., Heise, J., et al. 1981, Space Sci. Rev., 30, 221
Mauche, C. 1999, ApJ, 520, 822
Mukai, K., Ishida, M., Osborne, J. P., et al. 1998, ASP Conf. Ser., 137, 554
Patterson, J. 1984, ApJS, 54, 443
Patterson, J., & Raymond, J. C. 1985, ApJ, 292, 550
Ramsay, G. 2000, MNRAS, 314, 403
Ritter, H. 1985, A&A, 148, 207
Rosen, S. R., Mason, K. O., & Córdova, F. A. 1988, MNRAS, 231, 549
Rosen, S. R., Mason, K. O., & Mukai, K. 1991, MNRAS, 249, 417
Schwope, A. D., Beuermann, K., & Thomas, H.-C. 1990, A&A, 230, 120
Singh, J., & Swank, J. 1993, MNRAS, 262, 1000
Siegel, N., Reinsch, K., Beuermann, K., van der Woerd, H., & Wolff, E. 1989, A&A, 225, 97
Vande Putte, D., Smith, R. C., Hawkins, N. A., & Martin, J. S. 2002, A&A, in press
Verbunt, F. 1987, A&AS, 71, 339
Vogt, N., Krzeminski, W., & Sterken, C. 1980, A&A, 85, 106
Warner, B. 1983, IAU Coll., 72, 155
Warner, B. 1987, MNRAS, 227, 23
Watson, M. G., Sherrington, M. R., & Jameson, R. F. 1978, MNRAS, 184, 79
Williams, R. E. 1980, ApJ, 235, 939
Wood, M. 1994, IAU Coll., 147, 612